# Supplementary Information

**Hollow cuboidal MnCo$_2$O$_4$ coupled with nickel phosphate: A promising oxygen evolution reaction electrocatalyst**

Adit Kumar Shah[a], Sourav Bhowmick[a], Devipriya Gogoi[b], Nageswara Rao Peela[b], Mohammad Qureshi[a]*

[a]Department of Chemistry, Indian Institute of Technology Guwahati, Assam, India – 781039

[b]Department of Chemical Engineering, Indian Institute of Technology Guwahati, Assam, India - 781039

*Corresponding Author

E-mail: mq@iitg.ac.in

**Experimental**

**Chemicals used**

Cobalt nitrate (Sigma Aldrich), manganese nitrate (Sigma Aldrich), ammonium fluoride (Sigma Aldrich), urea (Sigma Aldrich), nickel nitrate (Merck), sodium dihydrogen orthophosphate (Merck), Milli Q water (18.2 MΩ.cm$^{-2}$), Ethanol (TMEDA) were used as obtained.

**Synthesis and fabrication protocol of h-MCO**

Step-by-step fabrication of h-MCO/NiPi electrode is shown in figure S1. The h-MCO was synthesized over FTO through hydrothermal route. Co(NO$_3$)$_2$ (1.16 g), Mn(NO$_3$)$_2$ (0.71 g), urea (1.44 g) and NH$_4$F (0.37 g), were dissolved in 70 ml deionized water, and the solution was kept under stirring for 2 h. FTO in a teflon vessel was kept, facing up in a 100 ml teflon-lined autoclave. The area of FTO exposed to solution was controlled by putting polyimide tape over the FTO which can sustain very high temperature and pH. Only 1 x 1 cm$^2$ of FTO was kept exposed to solution. The above solution mixture was then transferred into the autoclave and kept in an oven at 150 °C for 24 h. Pink colored film was formed over FTO, and was washed with deionized water and ethanol. After drying at 100 °C , it was transferred to a muffle furnace and calcined at 450 °C for 3 h to form black coloured hallow cuboidal MnCo$_2$O$_4$.

**Deposition of NiPi over h-MCO (h-MCO/NiPi)**

NiPi layer was deposited over h-MCO through electrodeposition technique. In a typical synthetic procedure Ni(NO$_3$)$_2$.6H$_2$O (1 mmol) and NaH$_2$PO$_4$.H$_2$O (1 mmol) were dissolved in

100 ml 1:1 (v/v) water and ethanol mixture solution and the solution was kept stirring for 1 h. The three electrode cell (Ag/AgCl as a reference, Pt as a counter and FTO/ h-MCO as a working electrode) was used for deposition of NiPi layer over h-MCO. Cyclic voltammetry was performed at the scan rate of 10 mV/sec within the voltage range of -1.2 V to 0.4 V for different cycles. Sample was then washed with deionized water followed by drying overnight at 100 °C.
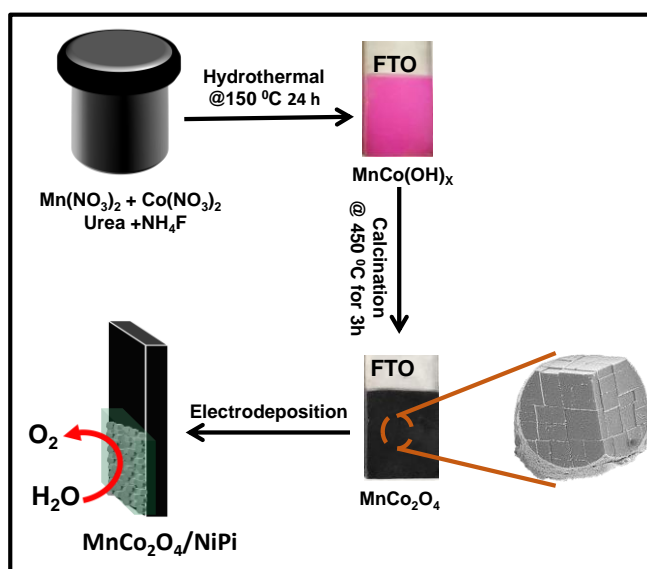


**Figure S1.** Step-by-step procedure for the green and cost effective fabrication of h-MCO/NiPi electrode directly over FTO.

## Materials characterization

X-ray diffraction measurements were carried out using Rigaku Smartlab X-ray diffractometer with Cu K$_\alpha$ ($\lambda$ = 1.54 Å), 9 kW power output. 514 nm laser excitation was used to perform Raman spectroscopy, using Horiba Jobin Vyon, Model LabRam HR. Morphological features of the samples were analysed using Field emission scanning electron microscopy (FESEM) in a Zeiss (model- Gemini and Sigma, operated at 5 kV) instrument. JEOL (JEM-2100F) Field emission transmission electron microscope (FETEM) with 200 kV operating voltage was used to record the transmission electron diffraction images. CH Instrument model CHI760E, Inc., Austin, TX was used to record electrochemical impedance spectroscopy (EIS). Gas chromatography (GC) (Model-7820A, Agilent Technologies) was used to measure the gas evolved/ Faradaic yield measurements. X-ray photoelectron spectroscopy (XPS) was done on Thermo Scientific (NEXA surface analysis with micro-focused, 72 W, 12 kV) with Al-K$_\alpha$ (h$\nu$ = 1486.6 eV) as X-ray source. The surface charging effect was compensated by referencing all

the peaks with respect to C 1s spectrum (284.77 eV). XPSPEAK 4.1 software was used for the study of core-level spectra. Stylus surface profilometer (Dektak 150) used for the measuring the thickness of thin films. Atomic absorption Spectrometer (AAS) measurement was done on Thermo Scientific (iCE 3000 AA01200816 v1.30) to quantify the amount of catalyst loaded.

**Electrochemical measurements:**

Electrochemical measurements were done with electrochemical analyser (model-CHI1120B) in a three-electrode system, using aqueous 1 M KOH (pH= 13) in a polypropylene electrochemical cell. Here, as-fabricated electrode was used as a working electrode, Pt as a counter electrode and Ag/AgCl as a reference electrode. At the scan rate of 1 mV/s, linear sweep voltammetry was carried out from 1.0 V to 2.0 V vs. RHE. EIS measurements were carried out at a frequency range from 0.1 Hz to 10 MHz. Following equation was used to convert applied potential using Ag/AgCl into RHE:

$$\text{E}_{RHE} = E_{Ag/AgCl}^{O} + 0.059pH + E_{Ag/Agcl} \tag{S1}$$

$E^{o}_{Ag/AgCl}$ = 0.1976 V at 25 °C, $E_{Ag/AgCl}$ is the potential measured against the Ag/AgCl reference electrode, $E_{RHE}$ is the potential vs. RHE, pH is the pH of electrolyte used.

Figure S2 (a) shows the powder X-ray diffraction (PXRD) pattern of h-MCO, NiPi and h-MCO/NiPi electrodes. Diffraction peaks of h-MCO were indexed to the corresponding (hkl) planes, confirming the formation of h-MCO, with no detectable impurity (JCPDS Card No - 00-023-1237). PXRD of NiPi, in figure S2 (a, ii) shows a broad peak in the range, 2ϴ (15-40) confirming the formation and amorphous NiPi. In the PXRD pattern of h-MCO/NiPi, all the peaks of h-MCO were indexed. Due to the amorphous nature of NiPi, diffraction peak of NiPi is not detectable in the composite as shown in figure S2 (a, iii). To further confirm the formation of electrocatalysts, h-MCO, NiPi and the composite h-MCO/NiPi, Raman spectra were recorded (figure S2 (b)). To further confirm the formation of electrocatalysts, h-MCO, NiPi and the composite h-MCO/NiPi, Raman spectra were recorded (figure S2 (b)). Raman bands at 186 cm⁻¹, 476 cm⁻¹, 522 cm⁻¹ and 675 cm⁻¹ corresponds to $F_{2g}$, $E_g$, $F_{2g}$ and $A_{1g}$ modes of spinel h-MCO, respectively. In the Raman spectrum of NiPi, a single band was observed

at 920 cm$^{-1}$, corresponds to symmetric O−P−O vibrational stretching mode which indicates formation of ($PO_4^{3-}$). The band at 951 cm$^{-1}$ for h-MCO/NiPi composite, confirms the presence of $PO_4^{3-}$ in h-MCO/NiPi catalyst, shift in $PO_4^{3-}$ towards higher binding energy indicates an electronic interaction between h-MCO and NiPi in h-MCO/NiPi composite.
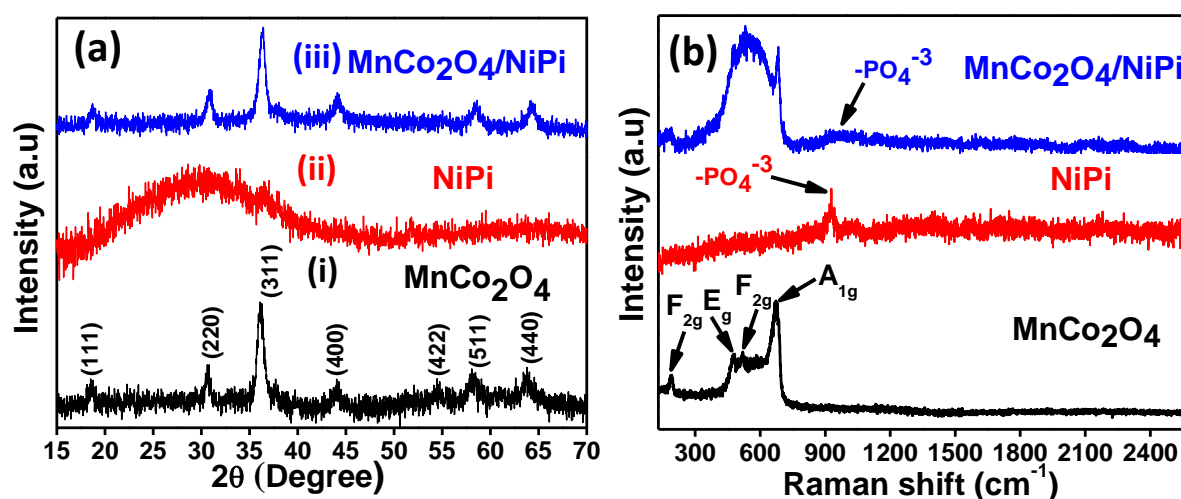


**Figure S2. (a)** Powder X-ray diffraction (PXRD) patterns of spinel h-MCO, amorphous NiPi and h-MCO/NiPi electrodes revealing the formation and purity of the respective catalysts, **(b)** Laser Raman spectra of spinel h-MCO, NiPi and the composite h-MCO/NiPi confirms the formation of electrocatalysts. Shift in $PO_4^{3-}$ towards higher binding energy indicates a good electronic interaction among h-MCO and NiPi in h-MCO/NiPi composite. Signature symmetric O−P−O vibrational stretching mode in the bare and the composite is indicative of nickel phosphate presence.

The survey spectra in figure S3 (a), confirms the presence of all the elements in $MnCo_2O_4$/NiPi, $MnCo_2O_4$ and NiPi electrodes. Figure S3 (b) shows the core level XPS spectra of P 2p for h-MCO/NiPi and NiPi, it de-convoluted to give $2p_{3/2}$ and $2p_{1/2}$ peaks at 133.25 eV and 134.10 eV in the composite, and at binding energies 133.12 eV and 134.07 eV in the bare NiPi electrode. It confirms the presence of phosphorus in phosphate form in both the electrodes.
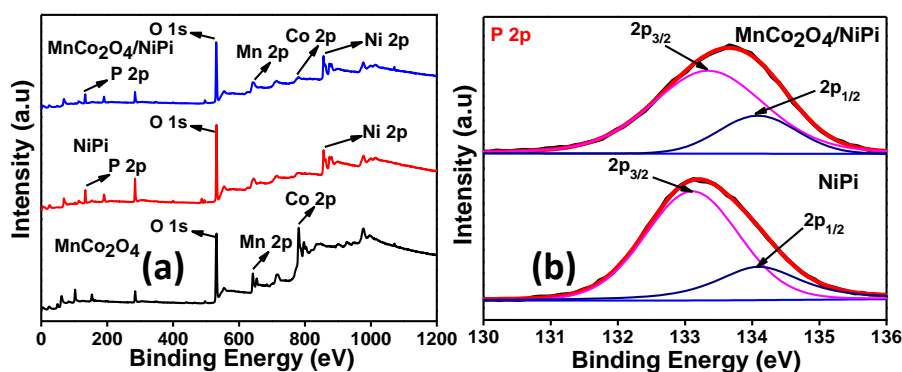
**Figure S3**. (a) XPS survey spectra of $MnCo_2O_4$/NiPi, $MnCo_2O_4$ and NiPi confirming presence of all the element present in the catalyst (b) P 2p core level spectra of h-MCO/NiPi, and NiPi confirms presence of phosphorus in phosphate form.

Figure S4 shows the optimised LSV curves of h-MCO/NiPi electrode at different cyclic voltammetry cycles of electrodeposited NiPi over h-MCO. h-MCO/NiPi electrode with five voltammetry cycles showing the best OER activity.
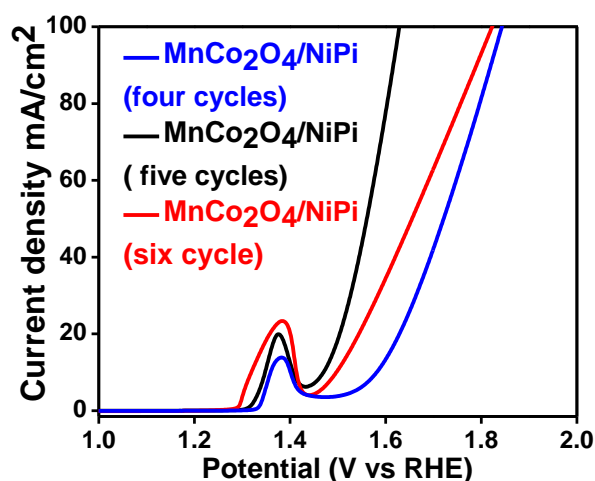


**Figure S4.** Shows the optimized Current density of $MnCo_2O_4$/NiPi electrode due to oxygen evolution reaction activity (OER), $MnCo_2O_4$/NiPi electrode with five cyclic voltammetry cycles is the most efficient electrode for activity among all.

To determine the electrochemical surface area (ECSA), which is an indicative of the number of electrochemical active sites in an electrocatalyst, cyclic voltammetry measurements of h-MCO and h-MCO/NiPi electrodes were done (shown in figure S5 (a, b)) in range of 0.0 - 0.06 V vs Ag/AgCl (non-faradic range) at different scan rates of 1-6 mV/sec. Double layer capacitance ($C_{dl}$), which gives a direct estimate of ECSA value, was calculated from the plot of the difference in current density ($j_{anode}$ - $j_{cathode}$ at 1.0 V vs RHE) of h-MCO/NiPi

and h-MCO electrodes against the scan rate of the slope, where $C_{dl}$ is equal to half of the slope value.
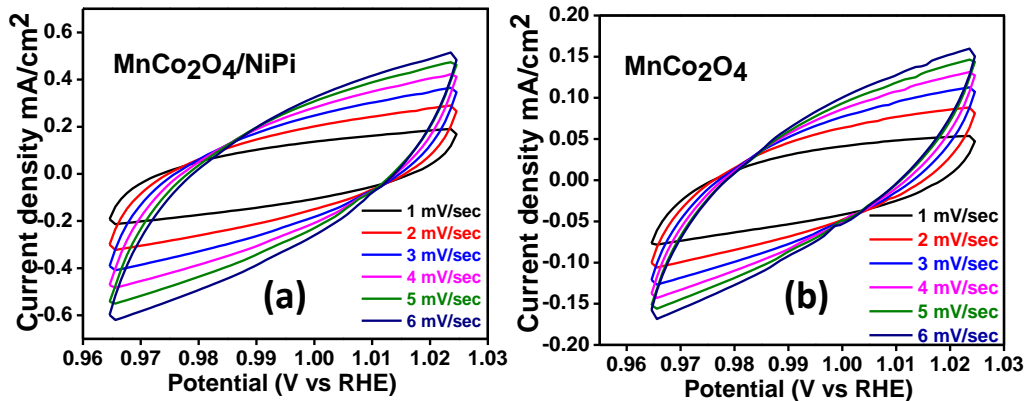


**Figure S5.** Cyclic voltammetry plots at different scan rates under alkaline conditions in a three electrode electrochemical cell in non-faradaic region of the respective catalysts (a) Bare h-MCO, (b) h-MCO/NiPi composite.

To determine the number of oxygen molecules formed from the active sites of the catalyst per unit time, turnover frequency (TOF) number was calculated at an operating potential of 1.53 V vs RHE shown in Figure S6. But to determine the TOF for OER, first the concentration of active sites ($N_S$) need to be quantified. The oxidation current in a CV measurement of the redox species was plotted against different scan rates, where they show a linear relationship, slope of which can be calculated using the equation

$$\text{Slope}(\frac{J_{anodic}}{Scan\,rate}) = n^2F^2AN_S/4RT \tag{S2}$$

Where n, R, and T are the number of electrons transferred, ideal gas constant and absolute temperature, respectively. TOF then can be calculated using the formula

$$\text{TOF} = \frac{J \times A}{n \times F \times N_S} \tag{S3}$$

where J, A, n, F, and $N_S$ are, current density at particular overpotential ($A/cm^2$), surface area of the electrocatalyst ($cm^2$), number of electrons transferred to evolve a molecule of $O_2$, Faraday constant (96458 C/mol), and concentration of active sites of the electrocatalysts ($mol/cm^2$) calculated from equation S2, respectively.

To understand, whether the gas evolved during the process is solely due to water oxidation and not due to the possible side reactions/products, Faradaic yield measurements were performed. Faradaic yield measurements were performed chronoamperometrically in

1 M KOH at an applied potential of 1.46 V vs RHE for 2 h and the gas evolved was monitored through an online-GC. The Faradaic yield was calculated using equation S4 along with the amount of gas evolved (calculated using equation S5) during the electrocatalytic process. The equation to calculate the Faradaic yield is

$$\text{Faradaic yield} = \frac{(\text{amount of gas evolved measured experimentally})}{(\text{amount of gas calculated theoretically})} \qquad (S4)$$

The amount of gas evolved were calculated using the formula

$$Amount\ of\ gas\ evolved = \frac{(J.t)}{(n.F)} \qquad (S5)$$

Where J is the current density (A/cm$^2$), t is the time (sec), n is the number of moles charge required to produced one mole of gas and F is the Faraday constant 96485(C (eN$_A$)).
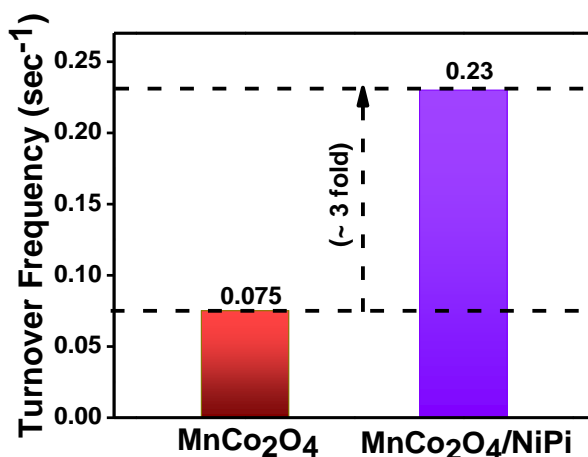


**Figure S6.** Turnover frequency (TOF) calculations show ~3 fold enhancement in TOF of h-MCO/NiPi composite in comparison to it bare counterpart, h-MCO.

Cyclic voltammogram in figure S7 (a, b) shows stability test till 1000 cycles of CV measurement for h-MCO/NiPi and h-MCO respectively, at the scan rate of 10 mV/sec in the non-faradaic region (0.0 - 0.06 V vs Ag/AgCl). Figure S7 (c, d) shows current density of the composite h-MCO/NiPi and bare h-MCO measured before and after 1000 cycles of CV displays insignificant change in current density which confirms the stability of both the electrodes.
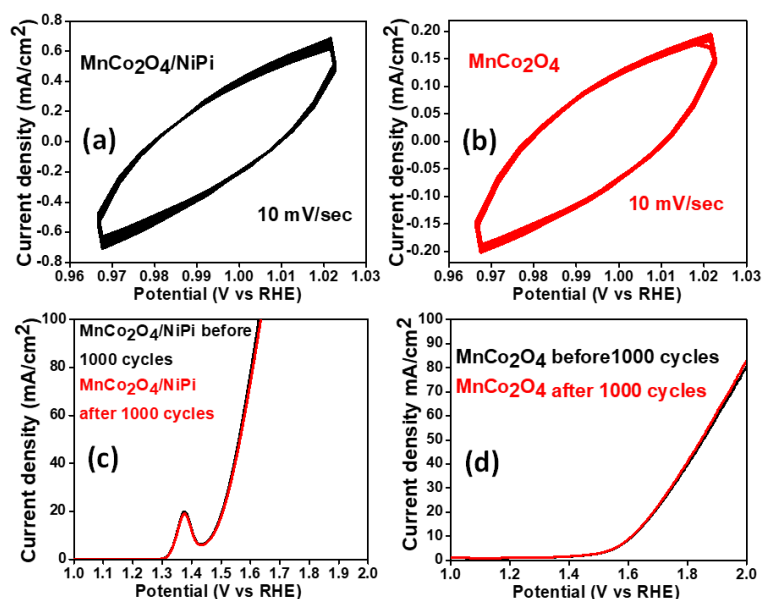
**Figure S7.** To check the stability of the MnCo₂O₄/NiPi catalyst and its bare counterpart. (a, b) 1000 cycles of cyclic voltammetry of MnCo₂O₄ and MnCo₂O₄/NiPi respectively at the scene rate of 10 mV/sec in a non-faradic region, (c, d) Current density of composite MnCo₂O₄/NiPi and bare MnCo₂O₄ measured before and after 1000 cycles of CV displays very insignificant change in current density which confirms the stability of both the electrodes.

Fourier-transform infrared (FTIR) spectroscopy measurement was performed to determine the formation of NiPi and the composite, shown in figure S8.The presence of two strong bands at 560 cm⁻¹ and 640 cm⁻¹ was attributed to the vibrational bending modes of Mn-O and C-O in the spinel MnCo₂O₄, respectively.[S1] In the FTIR spectra of NiPi, vibrational bands of PO₄⁻³ anion are observed around 1035 cm⁻¹, 1112 cm⁻¹ indicating formation of NiPi.[S2] Further in the FTIR spectra of h-MCO/NiPi, vibrational bending modes of manganese oxide and cobalt oxide in the spinel MnCo₂O₄ and vibrational bands of PO₄⁻³ anion was observed, which confirms the formation of the composite.
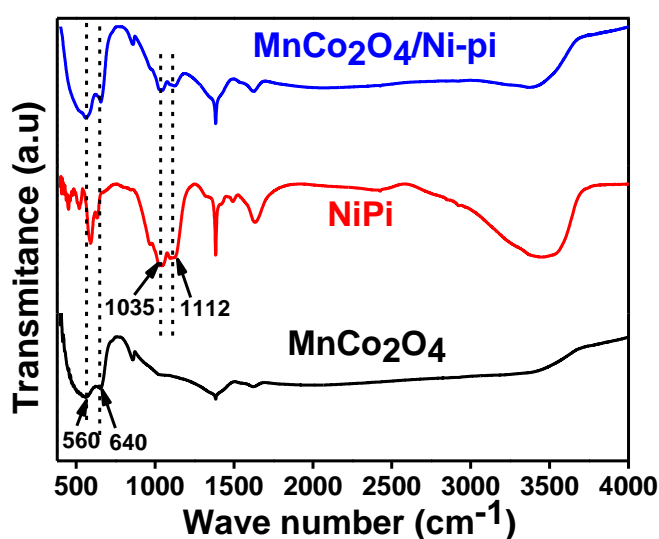


**Figure S8.** Fourier-transform infrared (FTIR) spectra of h-MCO/NiPi, h-MCO and NiPi.

Atomic absorption spectroscopy (AAS) measurement was done to quantify the amount of h-MCO and NiPi loading in h-MCO/NiPi electrode. In a typical experiment, 1x1 cm2 of h-MCO/NiPi electrode was digested in 7ml aqua regia (1:3, $HNO_3$:HCl) and 2 ml of sample solution was further diluted to 10 ml in deionized water. The sample solution was then filtered (using 0.22 $\mu$m syringe filter) and AAS measurement was done to determine the amount of h-MCO and NiPi loading in the composite as shown in table S1. To compare the activity of h-MCO/NiPi with benchmark catalyst, same amount of $RuO_2$ was taken and its liner sweep voltammetry was performed under similar experimental condition.

| Electrocatalyst | Mass Loading (mg/cm$^2$) |
|---|---|
| h-MCO | 1.26 |
| NiPi | 0.12 |

**Table S1.** Showing amount of H-MCO and NiPi loaded in the modified electrode h-MCO/NiPi.

To show the deposition and the good ohmic contact between h-MCO and the substrate, we have performed cross-sectional FESEM of the sample (Figure S9 (a). To further confirm the formation NiPi and the composite, we have performed selected area electron diffraction (SAED) of NiPi shown in the figure S9 (b). A characteristic amorphous nickel phosphate ring was observed, confirms the formation of NiPi. SAED pattern of h-MCO/NiPi shown in figure S9 (c), which can be assigned to the (220), (400) and (422) planes of h-MCO. Additionally, a characteristic NiPi ring was also observed confirming the formation of the composite.
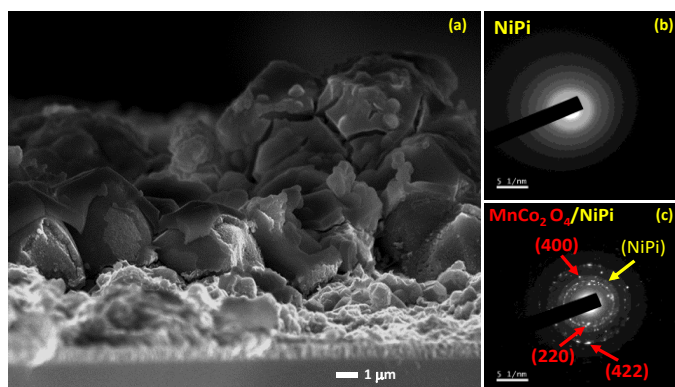


**Figure S9.** (a) Cross-sectional FESEM image of the composite showing deposition of NiPi over h-MCO, selected area electron diffraction (SAED) patterns of (b) NiPi, (c) h-MCO/NiPi.

In figure S10 (a), on application of potential across bare h-MCO, $Co^{2+}$ is being oxidised to $Co^{3+}$ and $Mn^{3+}$ to $Mn^{4+}$ and vice-versa. Figure S10 (b) shows the cyclic voltammetry of h-MCO/NiPi electrode where the formation of the redox couple $Ni^{2+}$/ $Ni^{3+}$ is confirmed.
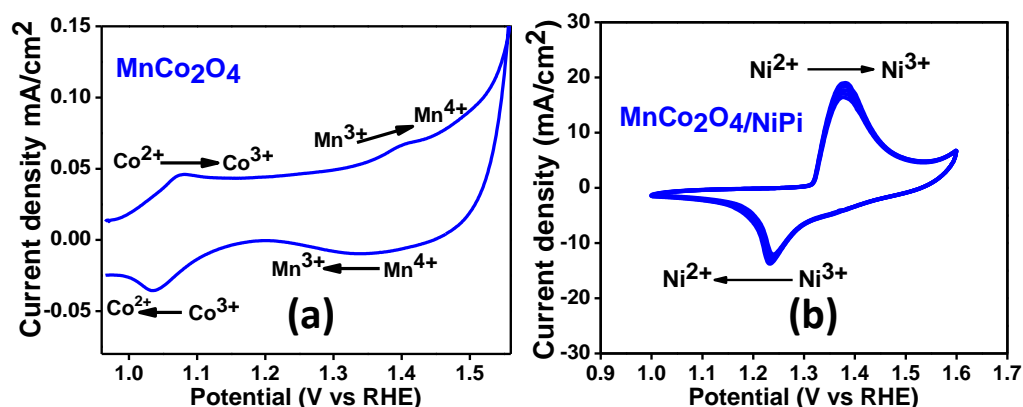


**Figure S10** (a) Cyclic voltammogram showing ($Co^{2+}$/ $Mn^{3+}$ $\leftrightarrow$ $Co^{3+}$/$Mn^{4+}$) redox cycle in bare h-MCO (b) Cyclic voltammogram showing ($Ni^{2+}$ $\leftrightarrow$ $Ni^{3+}$) redox process.

Herein we have compared the OER performance of h-MCO with two different phosphates, namely, NiPi and $Co_3(PO_4)_2$ (CoPi), where the loading amount of both the phosphates were kept same. Figure S11 (a) and S11 (b) shows the linear sweep voltammetry (LSV) measurements and Tafel slop respectively. The electrochemical performance of Nickel and cobalt phosphates, when coupled with h-MCO are shown in figure S11 (a). $\eta_{10}$ of h-MCO/NiPi was found to be 230 mV, while for h-MCO/CoPi, $\eta_{10}$ was 275 mV. The performance at $\eta_{10}$ is distinctly higher for NiPi. Moreover, the value of kinetics in terms of Tafel slop value favours nickel phosphate over cobalt phosphate in the present system, i.e. when coupled with h-MCO. For h-MCO/NiPi and MCO/CoPi, Tafel slopes were found to be 57 mV/dec and 99 mV/dec respectively, which shows h-MCO shows better OER kinetics when coupled with NiPi.
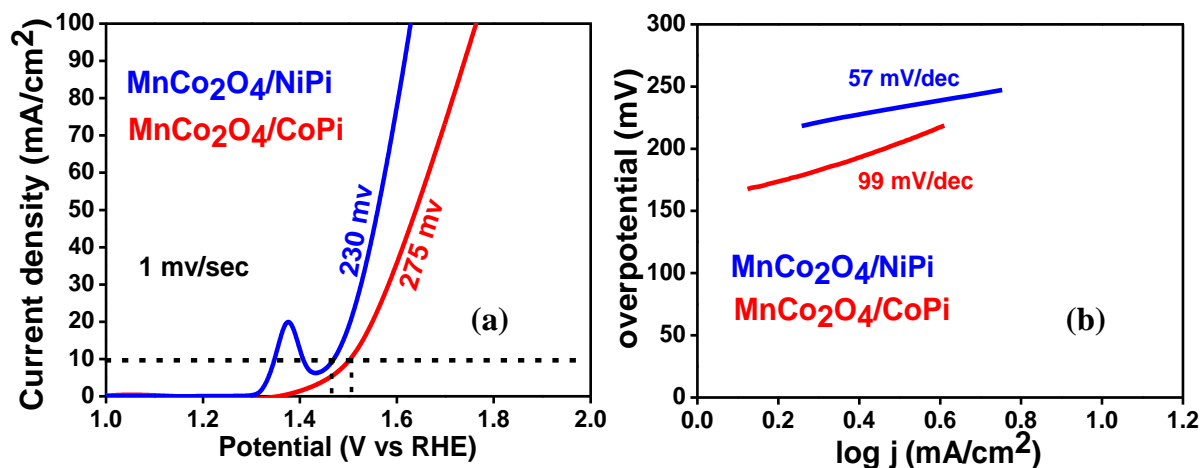
**Figure S11.** (a) Linear sweep voltammetry (LSV) plot, (b) Tafel plots, of h-MCO/NiPi and h-MCO/CoPi.

Figure S12 shows the Tauc plot of h-MCO/NiPi, displaying calculated band gap of the h-MCO/NiPi to be 3.58 eV.
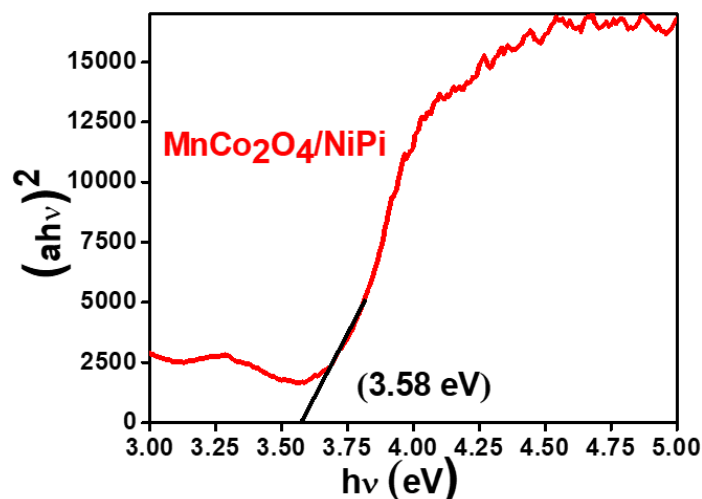


**Figure S12.** Tauc plot of h-MCO/NiPi showing band gap of composite.

## Comparison Table

| Catalyst | substrate | Overpotential (mV) at specific current density | Tafel slope (mV/dec) | Reference |
|---|---|---|---|---|
| **MnCo$_2$O$_4$/NiPi** | **FTO** | **230** | **57** | **This work** |
| MnCoP@MnCo$_2$O$_4$/Ti | Ti-mesh | 269 @(10mA/cm$^2$) | 102 | S3 |
| Mn$_2$O$_3$ + Co$_3$O$_4$ | Glassy carbon electrode | 400 @(10mA/cm$^2$) | 103 | S4 |
| P-MnCo$_2$O$_4$ | glassy carbon electrode | 349 @(10mA/cm$^2$) | 69.68 | S5 |
| MnCo$_2$O$_4$ | Glassy carbon electrode | 510 @(10mA/cm$^2$) | 123 | S6 |
| MnCo$_2$O$_4$-NW | Carbon cloth | 366 @(10mA/cm$^2$) | 197 | S7 |
| Mn$_{1-x}$Ni$_x$Co$_2$O$_4$/rGO | glassy carbon electrode | 290 @(10mA/cm$^2$) | 78 | S8 |
| Ce-MnCo$_2$O$_4$ | glassy carbon electrode | 390 @(10mA/cm$^2$) | 125 | S9 |

| | | | | |
|---|---|---|---|---|
| dp-MnCo$_2$O$_4$ | glassy carbon electrode | 700 @(10mA/cm$^2$) | ___ | S10 |
| Mn−Co oxyphosphide | glassy carbon electrode | 370 @(10mA/cm$^2$) | 66 | S11 |
| MnCo$_2$O$_4$@CoS | Nickel foam | 270@(20mA/cm$^2$) | 139. 19 | S12 |
| Mn$_x$Co$_{3-x}$O$_4$ | Nickel foam | 327 @(10mA/cm$^2$) | 79 | S13 |

## References

S1  Y. Zhang, L. Q. Luo, Z. Zhang, Y. P. Ding, S. Liu, D. M. Deng, H. B. Zhao and Y. Chen, *J. Mater. Chem.* B, 2014, **2**, 529–535

S2  M.A. Al-Omair, A.H. Touny and M.M. Saleh, *J. Power Sources,* 2017, **342,** 1032–1039.

S3  J. R. Han, S. Hao, Z. A. Liu, A. M. Asiri, X. P. Sun and Y. H. Xu, *Chem. Commun.,* 2018, **54**, 1077-1080, doi.org/10.1039/C7CC08895G.

S4  W. Wang, L. Kuai, W. Cao, M. Huttula, S. Ollikkala, T. Ahopelto, A. P. Honkanen, S. Huotari, M. Yu and B. Geng, *Angew. Chem., Int. Ed.*, 2017, **56**, 14977–14981, doi.org/10.1002/anie.201708765.

S5  Electrochemical water splitting exploration of MnCo$_2$O$_4$, NiCo$_2$O$_4$ cobaltites. *New J. Chem.* 2020, **44**, 17679–17692, doi.org/10.1039/D0NJ04188B

S6  P. W. Menezes, A. Indra, N. R. Sahraie, A. Bergmann, P. Strasser and M. Driess, *ChemSusChem,* 2015, **8**, 164–171. doi.org/10.1002/cssc.201402699

S7  S. Hao and Y. C. Yang*, J. Mater. Chem. A,* 2017, **5**, 12091–12095, doi.org/10.1039/C7TA03198J.

S8  A. Rebekah, E. Ashok Kumar, C. Viswanathan and N. Ponpandian, *Int. J. Hydrogen Energy*, 2020, **45**, 6391–6403, doi.org/10.1016/j.ijhydene.2019.12.164

S9  X. Huang, H. Zheng, G. Lu, P. Wang, L. Xing, J. Wang and G. Wang, *ACS Sustainable Chem. Eng.*, 2019, **7**, 1169–1177, doi.org/10.1021/acssuschemeng.8b04814.

S10 X. Ge, Y. Liu, F. W. Goh, T. S. Hor, Y. Zong, P. Xiao, Z. Zhang, S. H. Lim, B. Li, X. Wang and Z. Liu, *ACS Appl. Mater. Interfaces*, 2014, **6**, 12684–1269, doi.org/10.1021/am502675c.

S11 B. Y. Guan, L. Yu,X.W.Lou, *Angew.Chem.* 2017, **129**, 2426–2429, doi.org/10.1002/ange.201611804

S12 X. Du, H. Su and X. Zhang, *Int. J. Hydrogen Energy,* 2019, **44**, 21637–21650, doi.org/10.1016/j.ijhydene.2020.03.188

S13  K. Lankauf, K. Cysewska, J. Karczewski, A. MielewczykGryn, K. G´´ornicka, G. Cempura, M. Chen, P. Jasinski and´ S. Molin*, Int. J. Hydrogen Energy*, 2020, **45**, 14867–14879, doi.org/10.1016/j.ijhydene.2020.03.188.